# SUBWAVELENGTH CORRUGATED SURFACES FOR PLANAR FOCUSING: A PARAMETRIC ANALYSIS

Alberto Bernardini[1], Letizia Chisari[2,3], Michele Murciano[1], Federico Vescovi[1], Pio F. Calogero[1], Enrico Ricciardi[3]

[1] *Department of Electronics, Information and Bioengineering, Politecnico di Milano, Italy*
[2] *Department of Engineering and Informatics, University of Sussex, United Kingdom*
[3] *Labirinti Acustici, Via Gian Francesco Pizzi 20, Milano, Italy*

This paper is a revised version of the authors' submitted manuscript that was peer-reviewed by at least two anonymous reviewers.



## Abstract

Subwavelength corrugated surfaces (SCSs) provide a compact and broadband approach for planar acoustic focusing, enabling efficient wavefront manipulation without relying on bulky curved or refractive elements. While the focusing capabilities of SCSs have been demonstrated experimentally and numerically, a systematic understanding of how geometric parameters influence focal efficiency and operational bandwidth is lacking. This work presents a parametric analysis of planar focusing SCS configurations, introducing the Focal Concentration Efficiency metric to quantify the fraction of acoustic power localized near the focal point. Simulations based on both a full-wave model and a reduced-order phased-array model are employed to explore the effects of groove number, spacing, and overall surface dimensions over a broad frequency range. The results reveal clear geometry-driven trends, highlighting intrinsic efficiency limits and providing practical guidelines for the design of compact, broadband SCS-based acoustic focusing devices.

**Keywords:** *acoustic metamaterials, subwavelength corrugated surfaces, planar acoustic focusing*

## 1. Introduction

Acoustic metamaterials and metasurfaces have emerged as powerful tools for controlling sound propagation beyond the limits of conventional materials. By exploiting subwavelength features, they enable advanced manipulation of acoustic waves, including anomalous reflection, beam steering, and wavefront shaping [1], [2], [3], [4]. Compared to bulk metamaterials, metasurfaces offer reduced thickness and enhanced integrability, making them attractive for practical implementations [3], [5]. Their operation is commonly based on spatially varying phase discontinuities, enabling precise control of reflected or transmitted wavefronts. This mechanism is described by the generalized Snell's law, which relates the imposed phase gradient to the propagation direction [6]. This has enabled functionalities such as directional sound control and extraordinary reflection [7], [8], [9].

Among these, acoustic focusing is particularly relevant, as it allows energy concentration without relying on bulky curved reflectors or refractive elements. Several metasurface-based approaches have been proposed, including impedance-matched designs [10], cavity-based phase manipulation [11], and structured flat lenses [12]. While these approaches demonstrate effective focusing capabilities, they often rely on complex geometries or exhibit limitations in terms of bandwidth and fabrication. Subwavelength corrugated surfaces (SCSs) represent a particularly simple and physically intuitive approach to planar acoustic focusing. In these structures, a rigid surface is patterned with grooves of spatially varying depth, each acting as a subwavelength waveguide operating below cut-off. The resulting phase delay enables broadband and dispersionless manipulation of the reflected wavefront. This concept has been demonstrated in SCS-based metasurfaces for wavefront shaping and focusing [13], [14]. The physical mechanism underlying wave control via subwavelength corrugations is also supported by earlier theoretical and experimental studies [15], [16].

Despite these advances, a systematic understanding of how geometric parameters influence focusing remains limited. Existing works primarily focus on specific designs or proof-of-concepts, without a comprehensive analysis of the role of key parameters such as groove number, spacing, and aperture size. In particular, the relationship between geometry, focal concentration efficiency, and operational bandwidth has not been

***Corresponding author:*** *l.chisari@sussex.ac.uk.*

quantitatively characterized.

The present work addresses this gap through a parametric investigation of planar acoustic focusing using SCSs. A quantitative metric is introduced to evaluate the spatial concentration of energy around a prescribed focal point. The analysis is based on both full-wave simulations and a reduced-order phased-array model, enabling systematic exploration of geometric scaling effects over a broad frequency range. The results provide insight into the trade-offs between aperture size, spatial discretization, and bandwidth, offering practical design guidelines and clarifying the limits of compact SCS-based acoustic focusing devices.

## 2. SCS-based Planar Focusing

### 2.1. Continuous Formulation

Planar acoustic focusing using a reflector can be formulated as a wavefront synthesis problem in which the phase of the reflected field is designed such that all contributions interfere constructively at a prescribed focal point. Consider a reflecting surface reached by a normally incident plane wave. Let $F = (x_0, y_0)$ denote the desired focal point in the acoustic field. The reflected phase distribution along the surface must compensate for the difference in propagation distance between each surface point and the focal point $F$. If $x$ denotes an arbitrary position along the reflecting surface, the continuous groove depth profile of the SCS can be expressed as [13]

$$h(x) = C - \frac{1}{2}\sqrt{(x - x_0)^2 + y_0^2} \tag{1}$$

where $C$ is a constant introduced to ensure that $h(x) > 0$. This results in a spatial phase distribution corresponding to a converging reflected wavefront focusing acoustic energy at the desired point $F$.

### 2.2. Spatial Discretization

In the practical realization of SCSs, the reflecting surface is patterned with a series of narrow grooves whose depths vary along the surface. When an acoustic wave interacts with the structure, a portion of the incident field enters each groove, propagates toward its bottom, and reflects back toward the exterior. The round–trip propagation at a generic groove $n$ introduces a phase delay $\phi_n = 2k_0 h_n$ where $h_n$ is the depth of the $n$-th groove, $k_0 = 2\pi/\lambda$ is the acoustic wavenumber and $\lambda$ is the wavelength. By appropriately selecting the groove depths, the discretized structure approximates the continuous phase distribution required for focusing. The performance of the resulting SCS hence depends on several geometric parameters represented in Fig. 1. These include: the spatial step between adjacent grooves $s$, the groove width $w < s$, the groove separator length $d = s - w$, the number of grooves $N$, and the surface width (or aperture) $L = Ns + d$.

### 2.3. Operating Frequency Range

The operating frequency range is governed by geometry-driven limits at both low and high frequencies. In order for grooves to operate as subwavelength waveguides that support only the fundamental mode, the condition $w < \lambda/2$ must be satisfied. Under this assumption, the upper frequency limit is set by the waveguide cut-off

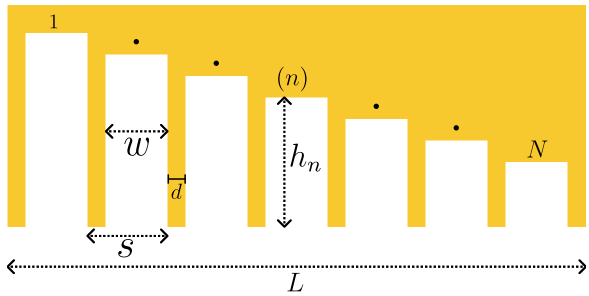


**Figure 1:** Geometric parameters of a generic SCS.

$$f_c = \frac{c_0}{2w}, \tag{2}$$

beyond which the subwavelength approximation breaks down. At low frequencies, the limitation is not abrupt but is instead governed by the finite aperture of the metasurface $L$. A characteristic lower operating bound can be estimated as

$$f_{\text{low}} \approx \frac{c_0}{2L} . \tag{3}$$

Below this frequency, the acoustic wavelength becomes too large compared to the metasurface aperture, and efficient focal concentration progressively deteriorates.

## 3. Definition of a Focusing Metric

In this work, a metric is introduced to quantify the spatial concentration of acoustic energy around the focal point. The metric is termed *Focal Concentration Efficiency* (FCE) and is mathematically defined as

$$\eta(f) = \frac{\displaystyle\int_\Omega G_F(x, y)\, |p(x, y, f)|^2 \, dx\, dy}{\displaystyle\int_\Omega |p(x, y, f)|^2 \, dx\, dy}, \tag{4}$$

where $\Omega$ denotes the spatial domain of interest, $p(x, y, f)$ is the scattered acoustic pressure field at position $(x, y)$ and frequency $f$, and $G_F(x, y)$ is a two-dimensional Gaussian window centered at the focal point $(x_0, y_0)$ with unit peak value and variance $\sigma^2$, expressed as

$$G_F(x, y) = \exp\left(-\frac{(x - x_0)^2 + (y - y_0)^2}{2\sigma^2}\right) . \tag{5}$$

The Gaussian window emphasizes the energy contribution in the vicinity of the focal point while smoothly attenuating that of more distant regions, with $\sigma^2$ controlling the effective spatial extent of the focal region. Since the absolute value of the metric $\eta$ depends on the size of the integration domain $\Omega$, the latter is kept fixed throughout the analysis to enable consistent comparisons across configurations.

## 4. SCS Modeling Approaches

To investigate the focusing performance of several SCS-based configurations, two complementary modeling approaches are considered. Full-wave simulations provide a high-fidelity description of the acoustic field, while a reduced-order phased-array model enables efficient exploration of the geometric parameters space.

### 4.1. Full-wave COMSOL model

Full-wave simulations are performed using COMSOL Multiphysics in the frequency domain. The SCS geometry is explicitly modeled as a rigid structure with sound-hard boundary conditions, and the surrounding domain is terminated with perfectly matched layers (PML) to avoid artificial reflections. The SCS is excited by a normally incident plane wave, and the resulting scattered acoustic field is computed over the domain of interest. This approach captures the full physical behavior of the system, including wave interactions within the grooves, boundary effects, and near-field phenomena, and is therefore used as a reference for evaluating focusing performance.

### 4.2. Phased Array model

A reduced-order phased-array model of the SCS behavior can be derived, in which the scattering of each groove is represented as a secondary source radiating into the acoustic domain, with phase determined by the corresponding groove depth [13]. The acoustic pressure field at a generic observation point $(x, y)$ is therefore expressed as the superposition of contributions from a uniform linear array of phase-controlled sources distributed along the metasurface with spacing $s$, such that the position of the $n$-th source is given by $x_n = ns$ [13]:

$$p(x, y, f) = \sum_{n=1}^{N} A_n \, e^{i\phi_n} \, H_0^{(1)}(k_0 r_n) \,, \tag{6}$$

where $A_n$ is an amplitude coefficient (assumed uniform under plane-wave excitation, i.e., $A_n = A$), $\phi_n$ is the phase associated with the $n$-th groove, $H_0^{(1)}$ is the Hankel function of the first kind and order zero, and $r_n$ is the distance between the observation point and the $n$-th groove. Further details of this phased-array model are provided in [13].

### 4.3. Efficiency Comparison Between Models

The phased-array model is implemented in MATLAB to enable efficient evaluation of SCS configurations. Both the MATLAB and COMSOL simulations are tested under comparable conditions, using spatial samplings of similar resolution (approximately $4 \times 10^6$ points in both cases over a domain of 4 m in the $x$ direction and 3 m in the $y$ direction). Further details on the simulation setup and common modeling parameters are provided in Section 5. The comparison shows that the phased-array model achieves a computational speed-up of more than one order of magnitude (about 25 times faster) with respect to full-wave simulation, while maintaining comparable accuracy, especially within the frequency range of interest, namely between $f_{\text{low}}$ and $f_c$, where the phased-array model provides a good approximation of the focusing behavior. Minor discrepancies may arise, especially at high frequencies, due to higher-order effects and near-field interactions that are captured only by the full-wave model. Fig. 2 shows a representative focusing scenario in terms of the squared magnitude of the acoustic pressure field $|p(x, y, f)|^2$, illustrating the overall agreement between the MATLAB and COMSOL simulations. The normalized mean squared error (NMSE) between the two $|p(x, y, f)|^2$ fields is approximately 3%.

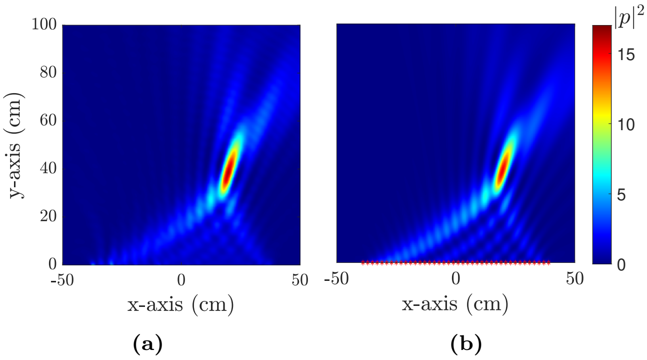


**Figure 2:** Simulation results with $F = (0.2\,\text{m}, 0.4\,\text{m})$, $s = 2$ cm and $N = 40$. Comparison between COMSOL (a) and phased-array model implemented in MATLAB (b).

## 5. Parametric Analysis

The proposed FCE metric is evaluated across a range of SCS configurations to assess the influence of geometric parameters on focusing performance. Unless otherwise specified, all simulations are carried out within the computational domain introduced in Subsection 4.3 and considering the same target focal point $F = (0.2\,\text{m}, 0.4\,\text{m})$. The groove width is fixed to $w = 2\,\text{cm}$ and the separator thickness to $d = 1\,\text{mm}$. The SCS is positioned at the center of the bottom boundary along the $x$-axis, and is excited by a normally incident plane wave of amplitude 1 Pa. For the Gaussian window, $\sigma = 0.015$. The FCE curves obtained from the two simulation approaches are nearly identical and exhibit the same frequency-dependent trends; therefore, the phased-array model is adopted due to its lower computational cost.

### 5.1. Effect of Number of Grooves

This study investigates the effect of varying the number of grooves $N$ while keeping the spatial step size $s$ fixed. Consequently, increasing $N$ proportionally enlarges the metasurface width $L$, enabling the influence of aperture size on $\eta$ to be assessed. Fig. 3 shows six curves representing $\eta(f)$ for SCS configurations with $N$ ranging from 10 to 60. A clear trend emerges, with FCE increasing as $N$ grows. A larger aperture captures a larger portion of the incident plane wave

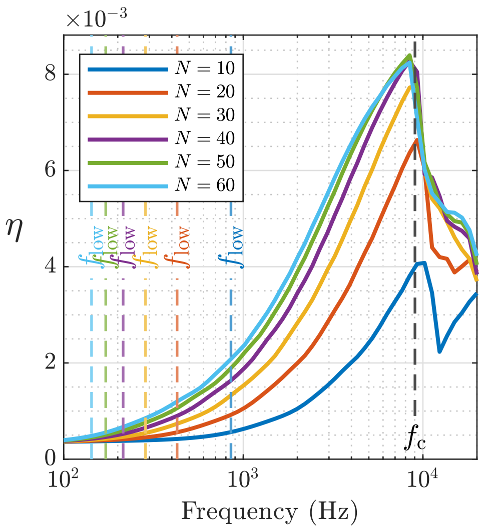


**Figure 3:** FCE curves for varying number of grooves $N$ with fixed step size $s = 2$ cm.

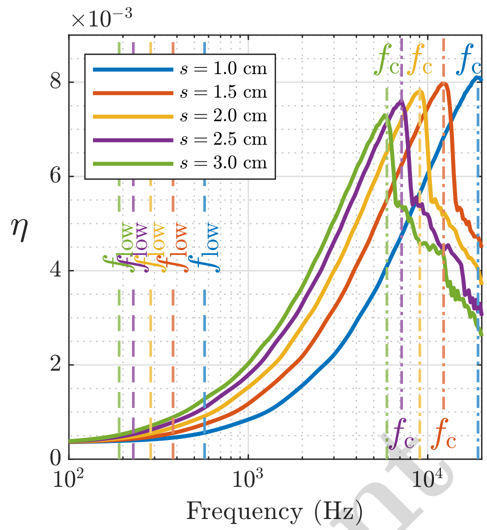


**Figure 4:** FCE curves for varying step size $s$ with constant number of grooves $N = 30$.

and redirects it toward the focal region. However, the curves for $N = 50$ and $N = 60$ nearly overlap, indicating diminishing returns as $L$ becomes sufficiently large. The lower bound $f_{\mathrm{low}}$ shifts towards lower frequencies with increasing $N$, consistent with its dependence on the total aperture $L$, as larger structures interact more effectively with longer wavelengths. At high frequencies, all configurations exhibit a similar drop in efficiency, occurring around the same frequency $f_c$.

### 5.2. Effect of Spatial Step Size

This set of experiments investigates the focusing performance as a function of the spatial step size $s$, while keeping the number of grooves $N$ fixed. Varying $s$ simultaneously affects the spatial discretization of the phase profile and the overall metasurface length $L$. Increasing $s$ leads to a proportional expansion of the aperture, enabling the metasurface to interact with longer acoustic wavelengths; consequently, the frequency bound $f_{\mathrm{low}}$ shifts toward lower frequencies. However, a larger step size leads to a coarser discretization of the phase profile, reducing accuracy and shifting the high-frequency limit $f_c$ towards lower values. Therefore, as shown in Fig. 4, a clear trade-off emerges: smaller values of $s$ provide finer phase resolution, higher FCE peaks at high frequencies and extend the high-frequency operating range, while higher values of $s$ increase the effective aperture, thus increasing the focusing performance at low frequencies.

### 5.3. Constant-Width Configurations

To isolate the effect of spatial discretization from that of the SCS size, this third analysis considers simultaneous variations of $N$ and $s$ such that $L$ remains constant. As shown in Fig. 5, in the low-frequency regime, all FCE curves nearly coincide and share the same lower bound $f_{\mathrm{low}}$, confirming that the behavior at low frequencies is predominantly determined by $L$. Conversely, as the step size $s$ decreases and $N$

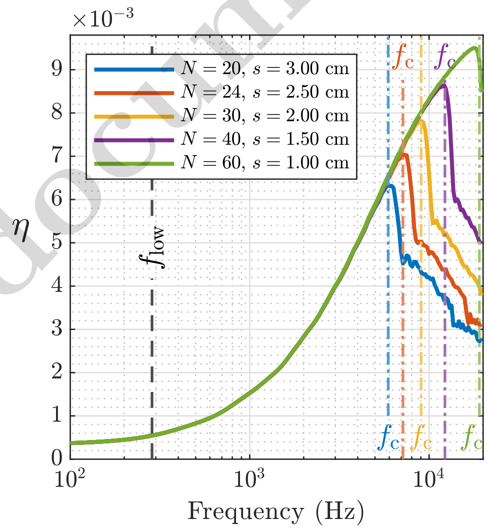


**Figure 5:** FCE curves for varying step size $s$ and number of grooves $N$, while maintaining fixed aperture $L = 60$ cm.

increases, the high-frequency limit $f_c$ shifts to higher frequencies, indicating that the upper bound is controlled by the spatial resolution of the discretized phase profile. It is worth noticing that more densely spatially sampled configurations generally achieve a broader operating bandwidth and higher FCE peaks.

### 5.4. Spatial Variation of Focusing Point

This study investigates how the FCE varies with the position of the focal point, parameterized by the radial distance $R$ of the focal point with respect to the midpoint of the SCS and the steering angle $\theta$. The considered positions of the focal point are shown in Fig. 6. Figures 7 and 8 show that the FCE decreases as either $R$ or $\theta$ increases, indicating reduced focusing performance for more distant and more off-axis focal points. For a fixed steering angle, larger radii lead to weaker focusing, whereas for a fixed radius, increasing $\theta$ progressively penalizes the energy concentration at

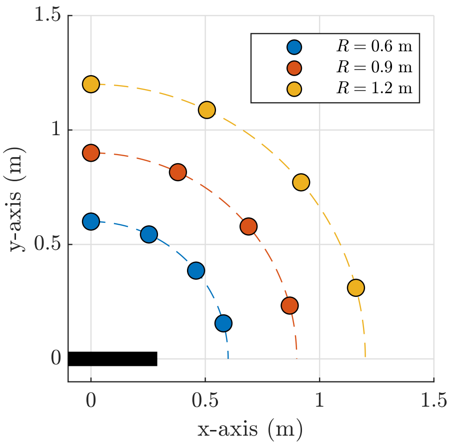


**Figure 6:** Half of the simulation domain containing target focal points located on three circular arcs of increasing radius $R$, centered at the surface midpoint, at steering angles of $0°, 25°, 50°$, and $75°$.

the target point.
Moreover, the FCE drop does not always occur in the immediate vicinity of $f_c$, and its onset is found to depend on the spatial location of the focal point, especially for small radii and large steering angles. This suggests that, while $f_c$ remains a useful geometry-based indicator of the high-frequency operating limit, the effective degradation of focusing performance is also influenced by the focal point location.

### 5.5. Frequency Dependence of Focal Area

Across all the configurations considered, the focal area was observed to depend strongly on frequency. Within the operating range, higher frequencies produce a more compact concentration of acoustic energy around the focal point, whereas lower frequencies lead to a progressively broader focal region. This behavior is consistent with an increase in the acoustic wavelength as the frequency decreases.

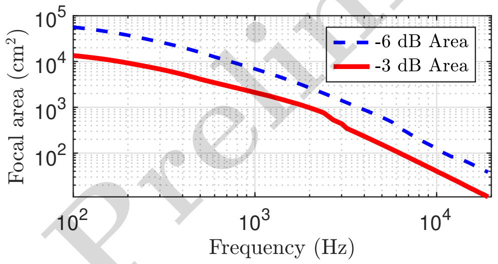


**Figure 9:** Focal area as a function of frequency.

To quantify this effect, the focal region was extracted from the simulated field using a region-growing image segmentation algorithm [17]. Starting from the focal point, the algorithm identifies the connected region in which the field amplitude remains within prescribed thresholds (here set to $-3$ dB and $-6$ dB) relative to its maximum value. The results shown in Fig. 9, referring to the configuration introduced in Subsection 4.3, clearly indicate that the high-amplitude focal area expands as frequency decreases. Similar trends were consistently observed across all the other simulated configurations. This behavior provides an additional spatial interpretation of the low-frequency degradation of focusing performance, complementing the FCE analysis described in the previous subsections.

## 6. Conclusions and Future Works

This work presented a parametric analysis of SCSs for acoustic focusing, highlighting the geometry-driven limits that affect their performance. A Gaussian-based metric, termed *Focal Concentration Efficiency* (FCE), was introduced to quantify the spatial concentration of acoustic energy around the focal point. The analysis showed how the FCE varies with the number of grooves, the spatial step size, the metasurface aperture, and the position of the focal point with respect to the SCS, while the focal area was found to broaden progressively as frequency decreases. Future work will address experimental validation and the extension of the present framework to more general focusing configurations.

## References


[1] M. Yang and P. Sheng, “Sound absorption structures: From porous media to acoustic metamaterials,” *Annual Review of Materials Research*, vol. 47, no. 1, pp. 83–114, 2017.

[2] D. Lee, D. M. Nguyen, and J. Rho, “Acoustic wave science realized by metamaterials,” *Nano Convergence*, vol. 4, no. 1, p. 3, 2017.

[3] B. Assouar, B. Liang, Y. Wu, Y. Li, J.-C. Cheng, and Y. Jing, “Acoustic metasurfaces,” *Nature Reviews Materials*, vol. 3, pp. 460–472, 2018.

[4] G. Liao, C. Luan, Z. Wang, J. Liu, X. Yao, and J. Fu, “Acoustic metamaterials: A review of theories, structures, fabrication approaches, and applications,” *Advanced Materials Technologies*, vol. 6, 2021.

[5] A. Zabihi, C. Ellouzi, and C. Shen, “Tunable, reconfigurable, and programmable acoustic metasurfaces: A review,” *Frontiers in Materials*, vol. 10, 2023.

[6] C. M. Li, S. Zhang, H. Chen, and W. Ye, “On the generalized snell’s law for the design of elastic metasurfaces,” *Journal of Applied Physics*, vol. 133, 2023.

[7] Y. Li, Z.-m. Gu, Z.-y. Zou, and J.-c. Cheng, “Reflected wavefront manipulation based on ultrathin planar acoustic metasurfaces,” *Scientific Reports*, vol. 3, 2013.

[8] Y. Li et al., “Experimental realization of full control of reflected waves with subwavelength acoustic metasurfaces,” *Phys. Rev. Appl.*, vol. 2, no. 6, 2014.

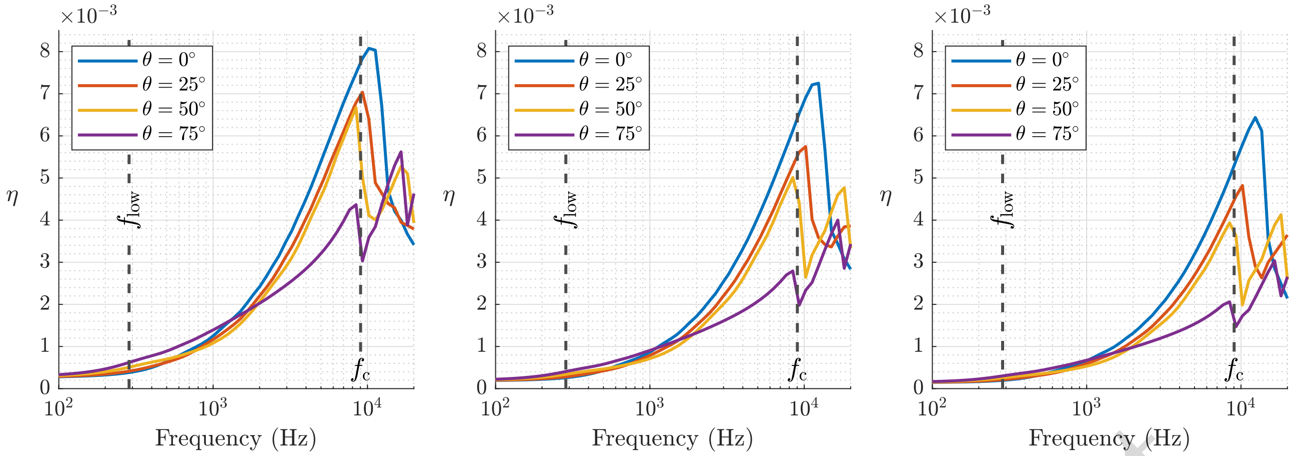


**(a)** $R = 0.60$ m **(b)** $R = 0.90$ m **(c)** $R = 1.20$ m

**Figure 7:** FCE curves for varying observation angle $\theta$ and different fixed radii. Other parameters are fixed to $N = 30$ and $s = 2$ cm. Radii are varied as follows in each subplot: (a) $R = 0.60$ m, (b) $R = 0.90$ m, and (c) $R = 1.20$ m.

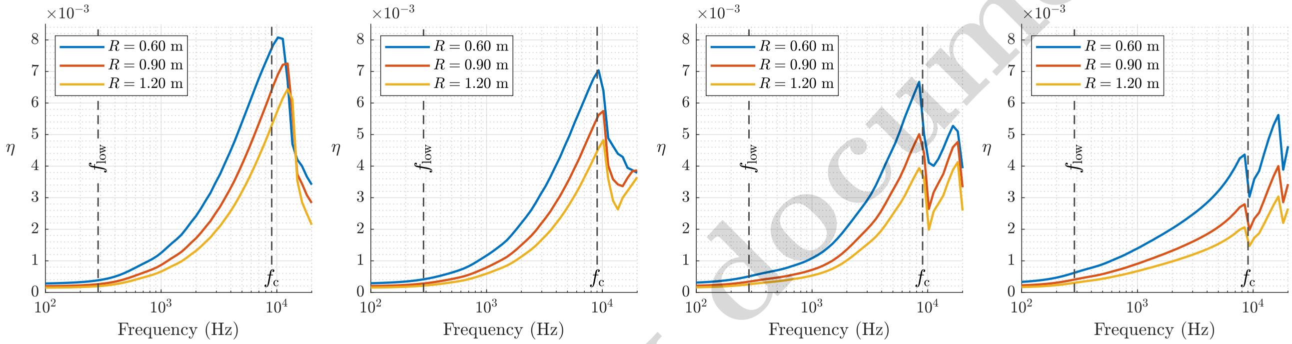


**(a)** $\theta = 0°$ **(b)** $\theta = 25°$ **(c)** $\theta = 50°$ **(d)** $\theta = 75°$

**Figure 8:** FCE curves for varying radius of the arc and different fixed steering angles. Other parameters are set to $N = 30$ and $s = 2$ cm. Angles are varied as follows in each subplot: (a) $\theta = 0°$, (b) $\theta = 25°$, (c) $\theta = 50°$, and (d) $\theta = 75°$.


[9] X.-P. Wang, L.-L. Wan, T.-N. Chen, A.-L. Song, and X.-W. Du, "Broadband reflected wavefronts manipulation using structured phase gradient metasurfaces," *AIP Advances Materials Technologies*, vol. 6, 2016.

[10] R. A. Jahdali and Y. Wu, "High transmission acoustic focusing by impedance-matched acoustic meta-surfaces," *Applied Physics Letters*, vol. 108, 2016.

[11] J. Qian, J. Xia, and H.-X. Sun, "Broadband acoustic focusing by cavity structures with phase manipulations," *Journal of Applied Physics*, vol. 122, no. 24, 2017.

[12] S. Gao, Q. Zeng, M. Gong, J. Lan, and X. Liu, "An acoustic flat lens for broadband focusing via cross-shape structure," *Micromachines*, vol. 14, no. 1, p. 12, 2023.

[13] Y.-F. Zhu et al., "Dispersionless manipulation of reflected acoustic wavefront by subwavelength corrugated surface," *Scientific Reports*, vol. 5, pp. 1–10, 2015.

[14] Y.-F. Zhu et al., "Multi-frequency acoustic metasurface for extraordinary reflection and sound focusing," *AIP Advances*, vol. 6, no. 12, 2016.

[15] J.-J. Wu, "Subwavelength microwave guiding by periodically corrugated strip line," *Progress In Electromagnetics Research*, vol. 103, no. 1, pp. 307–322, 2010.

[16] R. Lipton, A. Polizzi, and L. Thakur, "Novel metamaterial surfaces from perfectly conducting subwavelength corrugations," *SIAM Journal on Applied Mathematics*, vol. 77, no. 4, pp. 1316–1339, 2017.

[17] R. C. Gonzalez and R. E. Woods, *Digital Image Processing*, 4th ed. Pearson, 2018.